Stretching Nanowires on a Stretchable Substrate: A Method Towards Facile Fracture Testing and Elastic Strain Engineering

Felipe R. Poblete, Zheng Cui, Yuxuan Liu, Yong Zhu*

Department of Mechanical and Aerospace Engineering, North Carolina State University, Raleigh, NC 27695, USA

* Corresponding author. *E-mail address*: yong_zhu@ncsu.edu (Y. Zhu).

Abstract:

Nanomaterials are building blocks for a wide range of applications. They typically exhibit ultrahigh strength, which make them also promising candidates for elastic strain engineering. Here we demonstrate a facile method to measure fracture strain and strain distribution of nanomaterials, with Ag nanowires as an example. Nanowires are placed on top of or embedded in a stretchable substrate (i.e., elastomer), either as-prepared (van der Waals interactions) or treated with UV ozone (chemical bonding), which is subjected to uniaxial tensile loading. Nonlinear and bilinear cohesive shear-lag models can well capture the interfacial shear stress transfer characteristics associated with the two types of interactions, respectively. For each type, interfacial parameters such as stiffness, shear strength, and/or fracture toughness are identified by fitting the measured average strains of the nanowires. The nanowires embedded in as-prepared and on top of treated substrate are found to fracture under large substrate strain. The fracture strain and strain distribution along the nanowires are predicted using the shear-lag models. This method can be readily applied to investigate fracture and elastic strain engineering of 1D nanomaterials (regardless of aligned or inclined with respect to the stretching direction) and 2D nanomaterials.

Keywords:

Nanowires; Nanomechanics; Interfacial Mechanics; Fracture; Elastic Strain Engineering

1. INTRODUCTION

Nanomaterials such as nanowires exhibit ultrahigh strength and they are building blocks for a wider range of applications such as nanosensors, energy harvesting and storage, flexible and stretchable electronics, nanocomposites, and nanoelectromechanical systems [1–6]. For many of these applications, mechanical properties of nanomaterials are of important relevance. In particular, for flexible/stretchable electronics and nanocomposites, interfacial mechanics plays a key role. When the substrate or matrix is mechanically loaded, nanomaterials on top or within are loaded via interfacial shear stress transfer. It is important to know the fracture strain of the nanomaterials in order to design robust flexible/stretchable electronic devices and nanocomposites. Recently, elastic strain engineering has emerged as a promising way to tune, via mechanical strain, other physical and chemical properties of nanomaterials, where it is important to know precisely the strain distribution in the nanomaterials [7].

A number of methods have been developed to measure mechanical properties of 1D nanomaterials [8–11]. Atomic force microscopy (AFM) is commonly used to test fracture properties of individual nanomaterials in contact mode or lateral force mode, where the specimens can be either double clamped or cantilevered. However, for the contact mode, the AFM tip can slip off the specimen; for the lateral force mode, the force and displacement resolutions are relatively poor. Inside a scanning electron microscope (SEM), *in-situ* tensile testing of individual nanomaterials can be carried out using a customized manipulation and testing setup. More recently, *in-situ* tensile testing of individual nanomaterials has been performed inside a transmission electron microscope (TEM) using microelectromechanical system (MEMS) based testing stage [12–22]. In general, these tests for measuring fracture properties of 1D nanomaterials involve tedious specimen fabrication and/or manipulation process, which significantly limits the yield of such tests.

Elastic strain engineering of nanomaterials has received much interest recently as nanomaterials typically possess large yielding or fracture strain, offering unprecedented room for elastic strain engineering. Semiconductor nanowires have been found to exhibit pronounced change of electronic and optoelectronic properties under strain, such as bandgap, electron-hole recombination rate, and optical phonon frequency [8,23–25]. For metallic nanowires, axial strain or bending strain has been found to significantly affect the surface plasmon resonance [26,27]. So far three methods have been used to introduce strain in the nanowires: buckling a nanowire on an elastomer substrate [28,29] by releasing the prestrained substrate, bending a nanowire on a substrate [23–25] using a manipulator, and stretching a freestanding nanowire using a nanomechanical testing system [30]. In the first two methods the local strain is difficult to obtain, while in the third method the yield is low.

An alternative method is to stretch a substrate where nanomaterials, especially 2D materials, are placed either on top or embedded [31–34]. A nonuniform tensile strain is developed in the nanomaterial as a result of shear stress transfer. Typically, when the tensile strain in the nanomaterial is measured, with the aid of proper interfacial mechanics models the interfacial mechanical properties can be derived. Raman spectroscopy has been commonly used to measure the local strain, but the Grüneisen parameter characterizing relationship between strain and Raman shift must be obtained a priori, which would be challenging per se. In the case of nanowires, average axial strain measured using AFM can also be used to derive the interfacial mechanical properties. It is possible, with the known interfacial mechanical properties, to further predict the local strain distribution including fracture strain in the event of fracture, which, however, has not been explored.

Here we present a new and potentially facile method to measure fracture strain and strain distribution in the nanomaterials, with Ag nanowires as an example. Ag nanowires were aligned on top of or embedded in a polydimethylsiloxane (PDMS) substrate that was subsequently subjected to uniaxial tensile loading. The substrate was either as-prepared or treated with UV ozone (UVO) to examine the effect of van der Waals (vdW) interactions or chemical bonding. Nonlinear and bilinear cohesive shear-lag models were able to capture the interfacial shear stress transfer characteristics associated with the two types of interactions, respectively. For each type, the interfacial parameters such as stiffness, shear strength, and/or fracture toughness were identified by fitting the experimental results. Nanowires embedded in as-prepared and on top of treated substrate were found to fracture under the substrate stretching. The fracture strain and strain distribution along the nanowires were predicted using the shear-lag models with the identified interfacial parameters. We showed that inclined nanowires can be used too for studying fracture and elastic strain engineering after an equivalent strain applied to the PDMS substrate is calculated.

2. MATERIALS AND METHODS

2.1 Experiment

PDMS film with a thickness of about *0.3 mm* was prepared using Sylgard 184 (Dow Corning) by mixing the "base" and the "curing agent" with a ratio of 10:1. The liquid mixture was spin-coated on a silicon wafer and then thermally cured at $100\,^{o}C$ for *30 min*. After curing, the film was peeled off the silicon wafer and ready for testing "as-prepared". To prepare UVO-treated PDMS film, the as-prepared film was further treated using UVO Cleaner Model No. 42A (Jelight Company, Inc.) for *45 min*.

Ag nanowires were synthesized by the polyol method and diluted in ethanol with a concentration of *0.02 mg/ml*. These Ag nanowires, often called penta-twinned Ag nanowires, possess the fivefold twinned structure with five twin boundaries parallel to the nanowire axial direction [35]. The as-prepared Ag nanowire solution was dropped on a tilted PDMS film using a syringe. As the solvent flowed on the PDMS surface, the nanowires were mostly aligned along the flowing direction (Fig. 1). Samples with Ag nanowires embedded in PDMS were prepared in a similar fashion. The only difference was that after the Ag nanowires were dried on the PDMS surface, another layer of liquid PDMS was applied to seal the nanowires in the middle. The samples were then cured overnight at room temperature. Subsequently, as-prepared PDMS and UVO-treated PDMS with Ag nanowires on top or embedded were cut into 10×40 *mm* rectangular slabs. vdW interactions and chemical bonding are expected to exist between Ag nanowires and as-prepared PDMS and UVO-treated PDMS, respectively.

The slab samples were mounted onto a miniaturized mechanical testing stage (MTI Instruments, Inc.) for *in-situ* tensile testing under an optical microscope (Nikon LV150 with 100× objective and N.A. = 0.8). The loading rate was 10 μm/s. Each test was run continuously while the snapshots were taken periodically. As soon as a crack was observed, another snapshot was taken and the test was stopped (in the case of multiple fracture, the test would continue). It is an important advantage to run the test continuously without the need of stopping for taking images (e.g., in the case of AFM) [36]. By analyzing the sequence of optical images using digital image correlation (DIC), the Ag nanowire elongation and hence average axial strain can be obtained at each applied strain. An open-source DIC code [37] was used in this work, with the accuracy reported to be about 10% of a pixel [38,39]. Considering that the pixel size of the optical images is about *20 nm*, an accuracy of *2 nm* can be obtained.

2.2 Theory

In this work, nonlinear shear-lag and bilinear cohesive shear-lag models were employed to account for the vdW interactions and chemical bonding, respectively [40–44]. Due to symmetry of the problem, only half of the nanowire/PDMS system is considered. The nanowire has a half-length L with $x = 0$ at the center of the nanowire (Figs. 2a and c). For the nonlinear shear-lag model, the interface could consist of two zones: a bonded zone around the center ($x < L_1$) and a sliding zone emerging from the edge ($L_1 < x < L$), as shown in Fig. 2a. For the bilinear cohesive shear-lag model, the interface could consist of three zones: a bonded zone ($x < L_1$), a damaged zone ($L_1 < x < L_2$), and a debonded zone ($L_2 < x < L$), as shown in Fig. 2c. The key results of both nonlinear and bilinear cohesive shear-lag models are summarized below. For more details, please refer to our previous work [31,32,36].

For the nonlinear shear-lag model, the traction-separation law is shown in Fig. 2b, with two independent interface parameters, interfacial stiffness K_0 and shear strength τ_c. The critical substrate strain for onset of sliding is given by

$$\varepsilon_{c1} = \frac{\tau_c}{\beta E_{NW} h}\coth(\beta L) = \delta_1 \beta \coth(\beta L) \quad (1)$$

where E_{NW} is the Young's modulus of the nanowire, h the effective height, δ_1 the critical relative displacement between nanowire and substrate as shown in Fig. 2b, and $\beta = \sqrt{\frac{K_0}{E_{NW} h}}$ the shear-lag parameter. When $\varepsilon_m < \varepsilon_{c1}$, the entire nanowire is bonded to the substrate, and the axial strain in the nanowire is given by

$$\varepsilon(x) = \varepsilon_m\left(1 - \frac{\cosh(\beta x)}{\cosh(\beta L)}\right) \quad (2)$$

where ε_m is the strain applied to the substrate. The average strain in the nanowire is given by

$$\bar{\varepsilon} = \varepsilon_m\left(1 - \frac{tanh(\beta L)}{\beta L}\right) \quad (3)$$

When $\varepsilon_m > \varepsilon_{c1}$, the interface consists of two zones: a bonded zone and a sliding zone (Fig. 2a). The axial strain in the nanowire in the bonded zone and sliding zone are given by, respectively,

$$\varepsilon(x) = \varepsilon_m - \delta_1\beta\frac{\cosh(\beta x)}{\sinh(\beta L_1)} \quad (4a)$$

$$\varepsilon(x) = \frac{\tau_c}{E_{NW}h}(L - x) = \beta^2\delta_1(L - x) \quad (4b)$$

L_1 can be obtained by solving the following

$$\coth(\beta L_1) + \beta(L - L_1) = \frac{\beta E_{NW}h\varepsilon_m}{\tau_c} \quad (5)$$

The average strain in the nanowire is given by

$$\bar{\varepsilon} = \frac{\varepsilon_m L_1}{L} + \frac{\left(\beta^2(L-L_1)^2/2-1\right)\tau_c}{\beta^2 L E_{NW}h}\ when\ L_1 > 0 \quad (6a)$$

$$= \frac{\tau_c}{2E_{NW}h}L\ when\ L_1 = 0 \quad (6b)$$

For the bilinear cohesive shear-lag model, the traction-separation law is shown in Fig. 2d, with three independent interface parameters, interfacial stiffness K_0, shear strength τ_c, and mode II fracture toughness G. Two critical substrate strains, ε_{c1} and ε_{c2}, correspond to the onset of the damage and the debonding, respectively.

The first critical substrate strain ε_{c1} is still given by Eq. (1). When $\varepsilon_m < \varepsilon_{c1}$, the axial strain in the nanowire (all bonded to the substrate) is given by Eq. (2). When $\varepsilon_{c1} < \varepsilon_m < \varepsilon_{c2}$, the axial strain in the nanowire in the bonded zone is still given by Eq. (4a), while that in the damaged zone is given by

$$\varepsilon(x) = \varepsilon_m + A\alpha\sin\big(\alpha(x - L_1)\big) - B\alpha\cos\big(\alpha(x - L_1)\big) \quad (7)$$

where $\alpha = \sqrt{\tau_c/(E_{NW}h(\delta_2 - \delta_1))}$, $A = \delta_2 - \delta_1$, and $\mathrm{B} = \delta_1\beta\coth(\beta L_1)/\alpha$. L_1 can be obtained by solving the following

$$-\varepsilon_m = A\alpha\sin\big(\alpha(L-L_1)\big) - B\alpha\cos\big(\alpha(L-L_1)\big) \quad (8)$$

At the second critical substrate strain ε_{c2}, we have

$$A\cos\big(\alpha(L-L_1)\big) + B\sin\big(\alpha(L-L_1)\big) = 0 \quad (9)$$

This equation gives a critical value of L_1, at which ε_{c2} can be determined by Eq. (8).

When $\varepsilon_m > \varepsilon_{c2}$, the axial strain in the nanowire in the bonded zone and the damaged zone still take the same form of Eqs. (3a) and (6), respectively. In the debonded part, the axial strain in the nanowire becomes zero. The length of L_1 and L_2 can be obtained simply by solving Eqs. (8) and (9) simultaneously by substituting L with L_2.

The average strain in the nanowire is given by

$$\bar{\varepsilon} = \frac{\varepsilon_m L_2 - \delta_1}{L} + \frac{A\big(1-cos(\alpha(L_2-L_1))\big) - Bsin(\alpha(L_2-L_1))}{L} \; when\; L_1 > 0 \quad (10a)$$

$$= \frac{\varepsilon_m L_2}{L} + \frac{A\big(1-cos(\alpha L_2)\big) - Bsin(\alpha L_2)}{L} \; when\; L_1 = 0\; and\; L_2 > 0 \quad (10b)$$

$$= 0\; when\; L_2 = 0 \quad (10c)$$

Ag nanowires exhibit size dependent Young's modulus [35,45]. The Ag nanowires used in this study had diameters of ~60 nm, corresponding to a Young's modulus of ~90 GPa. Ag nanowires synthesized by the polyol method, as in this work, have a pentagonal cross section. When on top of the substrate, the nanowire/substrate interface is estimated to be one side surface of the nanowire cross section, corresponding to $h = \frac{1}{4}\sqrt{5\big(5+2\sqrt{5}\big)}a$ with a as the side width; when embedded in the substrate (matrix), the interface is the entire side surface of the nanowire cross section, corresponding to $h = \frac{1}{20}\sqrt{5\big(5+2\sqrt{5}\big)}a$.

3. RESULTS AND DISCUSSION

3.1 Nanowire on top of as-prepared PDMS

In this set of experiments, Ag nanowires were placed on top of as-prepared PDMS substrate. Most nanowires were aligned using the flow-assisted alignment method. The flow direction is the same as the subsequent loading direction. Three Ag nanowires parallel to the loading direction were tracked during the testing: NW #1 (*10.4 μm long*) and NW #2 (*12.4 μm*) on the same PDMS substrate, and NW #3 (*11.4 μm*) on a different PDMS substrate. Both PDMS substrates were stretched to a nominal strain of *30%* continuously, while the optical images of the nanowire(s) were taken at the increment of ~3% (Fig. 3a). The real strain applied to the PDMS can be measured by tracing some fixed features (e.g., particles as shown in Fig. 1a), which can be slightly different from the nominal strain. In addition, DIC was employed to obtain the average strain in the nanowire (from end to end), which is plotted against the applied strain to the PDMS substrate, as shown in Fig. 3b. As the DIC accuracy is 2 nm, the error in the average strain in the nanowire was estimated to be about ±0.02%.

VdW interactions are expected to occur at the interface of Ag nanowire and PDMS, therefore the nonlinear shear-lag model should be used to describe the interfacial shear stress transfer. Here, the nonlinear shear-lag model with the same two interfacial parameters – interfacial stiffness K_0 and shear strength τ_c – was used to fit the data of the three nanowires. The only differences between the three nanowires in the fitting were their dimensions including height and length. As shown in Eq. 6b, with the increasing applied strain to the substrate, the average nanowire strain approaches a plateau value, given by $\frac{\tau_c}{2E_{NW}h}L$. As it can be seen in Fig. 3b, the average strain in each of three nanowires did approach a plateau value, which then yielded the interfacial shear strength τ_c of 2.4±0.1 MPa (average of the three nanowires). Before sliding occurs, the average strain in the nanowire, as given in Eq. (3), is proportional to the applied strain with the proportional factor of

$1-\frac{sinh(\beta L)}{\beta L cosh(\beta L)}$, which should be able to yield the interfacial stiffness K_0. In view of the relatively large error for the data prior to sliding, K_0 for each nanowire was determined by fitting all the data points for the nanowire. The average value of K_0 is 6.0±0.4 TPa/m. The fitted interfacial stiffness K_0 and shear strength τ_c are listed in Table I.

Based on the fitted interfacial parameters, the axial strain distribution along any Ag nanowire can be predicted at a given applied strain to the PDMS substrate. Fig. 3c shows the NW #1 as an example. The peak strain, which occurs at the center of the nanowire, is about 0.22% when the PDMS strain is 25%. This finding can explain an interesting observation – none of the Ag nanowires fractured even though the applied strain to the PDMS substrate reached about 30%. For as-prepared PDMS, the bonding between Ag nanowire and PDMS is vdW interactions, which are relatively weak [46]. Hence, the interfacial shear stress transfer from PDMS substrate to Ag nanowire is not effective. As a result, all the nanowires tested in this case did not break.

3.2 Nanowire embedded in as-prepared PDMS

To enhance the interfacial shear stress transfer and potentially break the nanowires, we conducted another set of experiments where Ag nanowires were embedded in a PDMS substrate (matrix). This experiment is basically the same as the previous one. The only difference is that now the Ag nanowire has a larger contact area with PDMS (five side surfaces vs. one side surface), which should lead to a more effective interfacial stress transfer from substrate to Ag nanowire. Five Ag nanowires were tracked and analyzed (see Table 2), and two of them – NW #1 (*17.6 μm* long) and NW #2 (*20.3 μm* long) – are discussed here. Fig. 4a shows the loading process of NW #2. It was observed that the nanowire fractured when the PDMS strain was about *9.6%*. It was difficult to tell if the nanowire fully fractured or necked. It is known that while plasticity operates,

metallic nanowires typically exhibit brittle-like behavior. In other words, as soon as necking occurs the nanowire fractures rapidly [10,15,47]. Therefore, it is reasonable to take 9.6% as the fracture strain. The same nonlinear shear-lag model was used to predict the nanowire strain using the same interfacial parameters extracted from the previous experiments (i.e., K_0 of 6.0 TPa/m and τ_c of 2.4 MPa). Fig. 4b shows the comparison between the experimental data and the predicted data in the average strain of two Ag nanowires up to the fracture. Note that in the nonlinear shear-lag analysis, the Young's modulus of Ag nanowires was assumed to be constant (90 GPa), considering that plasticity is rather limited prior to fracture in Ag nanowires [35,47,48]. Overall the prediction agreed reasonably well with the experimental results. The error, $R_n = \sqrt{\frac{\sum_{i=1}^{N}(\varepsilon_i - \varepsilon_i')^2}{N}}$, was *7.4%* and *5.8%* for NW #1 and #2, respectively, where ε_i is the experimental data point, ε_i' is the predicted data point, and *N* is the number of data points. For the most part, it appears that the fitting slightly underestimates the average strain the nanowires. This might be due to the two reasons in the analysis: 1) assuming the constant Young's modulus of the Ag nanowires; 2) neglecting the interaction between the nanowire ends and the PDMS [49].

The axial strain in the embedded nanowire can be further predicted. Fig. 4c shows the axial strain distribution in NW #2. It can be seen that at the PDMS strain of *9.6%*, the peak strain in the middle of the nanowire is *1.97%*, which is taken as the fracture strain of NW #2. As shown in Fig. 4a, the nanowire fractured almost exactly in the middle, corroborating our analysis. The same analysis shows that the fracture of NW #1 was *1.72%*. The fracture strains of the five Ag nanowires are listed in Table 2. These fracture strain values are close to those reported in the literature for freestanding penta-twinned Ag nanowires, which is typically *2-3%* [35,48,50]. This is a reasonable agreement considering that fracture strain of a nanowire could depend on a number of factors such as nanowire diameter, preexisting defects, and loading rate [8]. It is well known that in freestanding

nanowires dislocation nucleation from the free surface is the dominant deformation mechanism [47,51–53]. It is unclear, however, if and how the nanowire/matrix interaction can alter the surface dislocation nucleation and hence the fracture strain, which warrants further investigation.

3.3 Nanowire on top of UVO-treated PDMS

In the third set of experiments, we employed another way to enhance the interfacial shear stress transfer, which was to place the Ag nanowires on a UVO-treated PDMS substrate. In this case, chemical bonds formed between Ag nanowire and UVO-treated PDMS are much stronger than the vdW interactions [54,55], which leads to a more effective interfacial stress transfer from the PDMS substrate to the Ag nanowires. Three Ag nanowires were tracked and analyzed, NW #1 (*11.6 μm* long), NW #2 (*14.4 μm* long), and NW #3 (*15.1 μm* long). Fig. 5a shows the loading process of NW #1 and NW #2. Fracture was first observed when the PDMS strain was about *5.3%*. Here, the cohesive shear-lag model [31,36] with the same three interfacial parameters – interfacial stiffness K_0, shear strength τ_c, and mode II fracture toughness G – was used to fit the data of the three nanowires. K_0 can be obtained first by fitting the initial slopes of the three nanowires to $1-\frac{sinh(\beta L)}{\beta L cosh(\beta L)}$. τ_c and G can be determined together by fitting all the data. The average values of the three nanowires, K_0 = *135.3±3.2 TPa/m*, τ_c = *22.5±1.2 MPa*, and G = *9.5±0.5 N/m* were obtained, as listed in Table 1.

Fig. 5c shows the axial strain distribution for NW #2. The peak strain in the middle of the nanowire is *2.07%* when the strain in the PDMS is *5.3%*. Similar to the embedded nanowire, the fracture occurred in the middle of the nanowire. The fracture strains for NW #1 and #3 were calculated to be *1.62%* and *2.13%*, respectively. Again, these values are within a reasonable range of the reported fracture strain of Ag nanowires. With further increase in the PDMS strain, NW #2

underwent a second fracture, further segmenting the original nanowire. Fig. 5d shows the predicted average strain, based on the fitted K_0, τ_c, and G, in the right segment of NW #2 (*7.3* μm long) from the first fracture up to the second fracture, along with the experimental data. The second fracture occurred when the strain in the PDMS was about *11.8%*. Fig. 5e shows the axial strain distribution for the right segment. It can be seen that the peak strain in the middle of the segment when the second fracture occurred was *1.18%*. It is interesting to observe that this value is relatively small when compared with the fracture strain values obtained previously and in the literature [35,48,50]. It is plausible that the mechanical behavior of the nanowires (e.g., surface dislocation nucleation) might be altered by the nanowire-PDMS interface, which is largely unknown at this point. Further work is warranted to provide a mechanistic understanding. The even smaller segments did not fracture further with the increasing PDMS strain. Figs. 5f and g show that the average strain and the peak strain in a segment were quite small (e.g., the peak strain no more than 0.6%), not sufficient to fracture the nanowire further.

3.4 Inclined nanowire on top of PDMS

With the flow-assisted alignment method, most Ag nanowires were aligned but some were inevitably inclined with respect to the flow (loading) direction. It was interesting to observe that the inclined nanowires remain straight during the loading to the PDMS substrate. Therefore, the inclined nanowires can be used to investigate fracture and elastic strain engineering too.

We found that when the PDMS substrate is stretched, an inclined nanowire deforms following a geometric compatibility with the substrate [56]. More specifically, the rectangular box bounding the nanowire, parallel to the loading direction, deforms and the inclined nanowire remains along the diagonal direction of the deformed box (Fig. 6a). Therefore, the analysis on the aligned

nanowires can be extended to the inclined ones, with the strain of the diagonal in the box (i.e., normalized length change of the diagonal) as the equivalent strain applied to the PDMS substrate. Assuming linear elasticity, the new nanowire angle and equivalent PDMS strain are given by, respectively,

$$\theta_1 = \tan^{-1}\frac{(1-\upsilon\varepsilon_m)\tan\theta_0}{1+\varepsilon_m} \tag{11a}$$

$$\varepsilon_{eq}(x) = \sqrt{\left(\sin\theta_0\,(1-\upsilon\varepsilon_m)\right)^2 + \left(\cos\theta_0\,(1+\varepsilon_m)\right)^2} - 1 \tag{11b}$$

where θ_0 is the initial inclined angle of the nanowire and υ is the Poisson's ratio of PDMS. For the strain range up to 30% in this study, linear elasticity yields very close results to hyperelasticity that can more accurately describe rubbery materials like PDMS [56]. Figs. 6b and c show the new inclination angle and the equivalent strain applied to the PDMS substrate, respectively, as functions of the initial inclination angle and the applied strain to the PDMS substrate. In this work the inclination angle is relatively small, mostly less than 10^o (as shown in Fig. 1a), and hence the equivalent strain is nearly equal to the strain applied to the PDMS. Take the example of 10^o, the equivalent strain is ~4% smaller than the strain applied to the PDMS.

Figs. 6d and e show the average strains of an Ag nanowire (*10 μm* long) on top of as-prepared and UVO-treated PDMS, respectively. As long as the equivalent strain applied to the PDMS substrate is obtained, the average strains of the nanowire and the strain distribution along the nanowire, for both as-prepared and UVO-treated PDMS, can be calculated following the theoretical analysis, as detailed in Eqs. 1-10.

To evaluate the accuracy of the analytical solutions for the inclined nanowire, finite element analysis (FEA) (ABAQUS, version 6.14) was employed to calculate the new inclination angle (Fig. 6b) and the average strains in the nanowire for both as-prepared and UVO-treated PDMS (Figs. 6d and e). The Ag nanowire was modeled with a pentagonal cross-section and having one

of its faces in contact with PDMS. C3D8R reduced linear brick elements were used to model both PDMS and Ag nanowire. Both materials are considered isotropic, linearly elastic with the following properties: Young's modulus *90 GPa* and 2MPa and Poisson's ratio 0.3 and 0.48, for Ag nanowire and PDMS [36], respectively. The diameter of the Ag nanowire for both cases was set as *60 nm*. The interface between Ag nanowire and PDMS was modeled using a surface-based cohesive contact approach [36]. A traction-separation law with the parameters given in Table I was used to describe the constitutive behavior of the interface. Close agreement can be found between the analytical and FEA results. Note that the accuracy of the analytical solutions for the aligned nanowire has been verified previously in the case of Si nanowires [36].

In addition to being inclined, some nanowires were observed to be slightly curved (e.g., NW#2 in Fig. 5a). We performed two groups of FEA simulations for comparison – one on a straight nanowire and the other on a curved nanowire – to account for the curvature effect in accordance with the experimental conditions (e.g., the nanowire dimensions, curvatures, 30% applied strain for the as-prepared PDMS, and 10% applied strain for the UVO-treated PDMS). The straight and curved nanowires showed negligible difference in the strain distribution.

4. CONCLUSIONS

We demonstrated a facile method to measure fracture strain and strain distribution in nanomaterials, with Ag nanowires as an example. Ag nanowires were aligned on top of or embedded in a PDMS substrate that was subsequently subjected to uniaxial tensile loading. The substrate was either as-prepared or UVO-treated to examine the effect of vdW interactions or chemical bonding. Nonlinear and bilinear cohesive shear-lag models were able to capture the interfacial shear stress transfer characteristics associated with the two types of interactions,

respectively. For each type, the interfacial parameters such as stiffness, shear strength, and/or fracture toughness were identified by fitting the measured average strains of the nanowires. The nanowires embedded in as-prepared and on top of treated substrate were found to fracture under the substrate stretching. The fracture strain and strain distribution along the nanowires were predicted using the shear-lag models with the identified interfacial parameters. We showed that inclined nanowires can be used too for studying fracture and elastic strain engineering after an equivalent axial strain on the PDMS substrate is calculated, as well as the slightly curved nanowires. This method can be readily applied to investigate fracture and elastic strain engineering of a wide variety of 1D and 2D nanomaterials.

ACKNOWLEDGEMENT

The authors gratefully acknowledge financial support from the National Science Foundation (NSF) through Award No. CMMI-1929646.

REFERENCES

[1] F. Xu, Y. Zhu, Highly conductive and stretchable silver nanowire conductors, Adv. Mater. 24 (2012) 5117–5122. https://doi.org/10.1002/adma.201201886.

[2] S. Yao, Y. Zhu, Wearable multifunctional sensors using printed stretchable conductors made of silver nanowires, Nanoscale. 6 (2014) 2353–2360. https://doi.org/10.1039/c3nr05496a.

[3] O.Y. Loh, H.D. Espinosa, Nanoelectromechanical contact switches, Nat. Nanotechnol. 7 (2012) 283–295. https://doi.org/10.1038/nnano.2012.40.

[4] J.Y. Lee, S.T. Connor, Y. Cui, P. Peumans, Solution-processed metal nanowire mesh

transparent electrodes, Nano Lett. 8 (2008) 689–692. https://doi.org/10.1021/nl073296g.

[5] Y. Xia, P. Yang, Y. Sun, Y. Wu, B. Mayers, B. Gates, Y. Yin, F. Kim, H. Yan, One-dimensional nanostructures: Synthesis, characterization, and applications, Adv. Mater. 15 (2003) 353–389. https://doi.org/10.1002/adma.200390087.

[6] Functional nanowires, MRS Bull. 32 (2007) 99–108. https://doi.org/10.1557/mrs2007.41.

[7] J. Li, Z. Shan, E. Ma, Elastic strain engineering for unprecedented materials properties, MRS Bull. 39 (2014) 108–114. https://doi.org/10.1557/mrs.2014.3.

[8] Y. Zhu, Mechanics of Crystalline Nanowires: An Experimental Perspective, Appl. Mech. Rev. 69 (2017). https://doi.org/10.1115/1.4035511.

[9] Y. Zhu, C. Ke, H.D. Espinosa, Experimental techniques for the mechanical characterization of one-dimensional nanostructures, Exp. Mech. 47 (2007). https://doi.org/10.1007/s11340-006-0406-6.

[10] G. Richter, K. Hillerich, D.S. Gianola, R. Mönig, O. Kraft, C.A. Volkert, Ultrahigh strength single crystalline nanowhiskers grown by physical vapor deposition, Nano Lett. 9 (2009) 3048–3052. https://doi.org/10.1021/nl9015107.

[11] L. Zhong, F. Sansoz, Y. He, C. Wang, Z. Zhang, S.X. Mao, Slip-activated surface creep with room-temperature super-elongation in metallic nanocrystals, Nat. Mater. 16 (2017) 439–445. https://doi.org/10.1038/NMAT4813.

[12] Y. Zhu, T.H. Chang, A review of microelectromechanical systems for nanoscale mechanical characterization, J. Micromechanics Microengineering. 25 (2015). https://doi.org/10.1088/0960-1317/25/9/093001.

[13] Y. Zhu, H.D. Espinosa, An electromechanical material testing system for in situ electron microscopy and applications, Proc. Natl. Acad. Sci. U. S. A. 102 (2005) 14503–14508.

https://doi.org/10.1073/pnas.0506544102.

[14] M.A. Haque, M.T.A. Saif, A review of MEMS-based miroscale and nanoscale tensile and bending testing, Exp. Mech. 43 (2003) 248–255. https://doi.org/10.1007/BF02410523.

[15] L.Y. Chen, M.R. He, J. Shin, G. Richter, D.S. Gianola, Measuring surface dislocation nucleation in defect-scarce nanostructures, Nat. Mater. 14 (2015) 707–713. https://doi.org/10.1038/nmat4288.

[16] R.A. Bernal, A. Aghaei, S. Lee, S. Ryu, K. Sohn, J. Huang, W. Cai, H. Espinosa, Intrinsic bauschinger effect and recoverable plasticity in pentatwinned silver nanowires tested in tension, Nano Lett. 15 (2015) 139–146. https://doi.org/10.1021/nl503237t.

[17] T.H. Chang, Y. Zhu, A microelectromechanical system for thermomechanical testing of nanostructures, Appl. Phys. Lett. 103 (2013). https://doi.org/10.1063/1.4858962.

[18] G. Cheng, S. Yin, T.H. Chang, G. Richter, H. Gao, Y. Zhu, Anomalous Tensile Detwinning in Twinned Nanowires, Phys. Rev. Lett. 119 (2017). https://doi.org/10.1103/PhysRevLett.119.256101.

[19] R. Ramachandramoorthy, W. Gao, R. Bernal, H. Espinosa, High Strain Rate Tensile Testing of Silver Nanowires: Rate-Dependent Brittle-to-Ductile Transition, Nano Lett. 16 (2016) 255–263. https://doi.org/10.1021/acs.nanolett.5b03630.

[20] C. Li, D. Zhang, G. Cheng, Y. Zhu, Microelectromechanical Systems for Nanomechanical Testing: Electrostatic Actuation and Capacitive Sensing for High-Strain-Rate Testing, Exp. Mech. 60 (2020) 329–343. https://doi.org/10.1007/s11340-019-00565-5.

[21] M. Naraghi, I. Chasiotis, H. Kahn, Y. Wen, Y. Dzenis, Novel method for mechanical characterization of polymeric nanofibers, Rev. Sci. Instrum. 78 (2007). https://doi.org/10.1063/1.2771092.

[22] D. Zhang, J.M. Breguet, R. Clavel, V. Sivakov, S. Christiansen, J. Michler, In situ electron microscopy mechanical testing of silicon nanowires using electrostatically actuated tensile stages, J. Microelectromechanical Syst. 19 (2010) 663–674. https://doi.org/10.1109/JMEMS.2010.2044746.

[23] E.M. Grumstrup, M.M. Gabriel, C.W. Pinion, J.K. Parker, J.F. Cahoon, J.M. Papanikolas, Reversible strain-induced electron-hole recombination in silicon nanowires observed with femtosecond pump-probe microscopy, Nano Lett. 14 (2014) 6287–6292. https://doi.org/10.1021/nl5026166.

[24] J. Chen, G. Conache, M.E. Pistol, S.M. Gray, M.T. Borgström, H. Xu, H.Q. Xu, L. Samuelson, U. Håkanson, Probing strain in bent semiconductor nanowires with raman spectroscopy, Nano Lett. 10 (2010) 1280–1286. https://doi.org/10.1021/nl904040y.

[25] X. Han, L. Kou, X. Lang, J. Xia, N. Wang, R. Qin, J. Lu, J. Xu, Z. Liao, X. Zhang, X. Shan, X. Song, J. Gao, W. Guo, D. Yu, Electronic and mechanical coupling in bent ZnO nanowires, Adv. Mater. 21 (2009) 4937–4941. https://doi.org/10.1002/adma.200900956.

[26] W. Wang, Q. Yang, F. Fan, H. Xu, Z.L. Wang, Light propagation in curved silver nanowire plasmonic waveguides, Nano Lett. 11 (2011) 1603–1608. https://doi.org/10.1021/nl104514m.

[27] H.S. Park, X. Qian, Surface-stress-driven lattice contraction effects on the extinction spectra of ultrasmall silver nanowires, J. Phys. Chem. C. 114 (2010) 8741–8748. https://doi.org/10.1021/jp100456p.

[28] F. Xu, W. Lu, Y. Zhu, Controlled 3D buckling of silicon nanowires for stretchable electronics, ACS Nano. 5 (2011) 672–678. https://doi.org/10.1021/nn103189z.

[29] L. Sun, D.H. Kim, K.H. Oh, R. Agarwal, Strain-induced large exciton energy shifts in

buckled CdS nanowires, Nano Lett. 13 (2013) 3836–3842. https://doi.org/10.1021/nl401860f.

[30] B. Wei, K. Zheng, Y. Ji, Y. Zhang, Z. Zhang, X. Han, Size-dependent bandgap modulation of zno nanowires by tensile strain, Nano Lett. 12 (2012) 4595–4599. https://doi.org/10.1021/nl301897q.

[31] G. Guo, Y. Zhu, Cohesive-Shear-Lag Modeling of Interfacial Stress Transfer between a Monolayer Graphene and a Polymer Substrate, J. Appl. Mech. Trans. ASME. 82 (2015). https://doi.org/10.1115/1.4029635.

[32] T. Jiang, R. Huang, Y. Zhu, Interfacial sliding and buckling of monolayer graphene on a stretchable substrate, Adv. Funct. Mater. 24 (2014) 396–402. https://doi.org/10.1002/adfm.201301999.

[33] Z. Dai, L. Liu, Z. Zhang, Strain Engineering of 2D Materials: Issues and Opportunities at the Interface, Adv. Mater. 31 (2019). https://doi.org/10.1002/adma.201805417.

[34] G. Wang, Z. Dai, L. Liu, H. Hu, Q. Dai, Z. Zhang, Tuning the Interfacial Mechanical Behaviors of Monolayer Graphene/PMMA Nanocomposites, ACS Appl. Mater. Interfaces. 8 (2016) 22554–22562. https://doi.org/10.1021/acsami.6b03069.

[35] Y. Zhu, Q. Qin, F. Xu, F. Fan, Y. Ding, T. Zhang, B.J. Wiley, Z.L. Wang, Size effects on elasticity, yielding, and fracture of silver nanowires: In situ experiments, Phys. Rev. B - Condens. Matter Mater. Phys. 85 (2012). https://doi.org/10.1103/PhysRevB.85.045443.

[36] F.R. Poblete, Y. Zhu, Interfacial shear stress transfer at nanowire-polymer interfaces with van der Waals interactions and chemical bonding, J. Mech. Phys. Solids. 127 (2019) 191–207. https://doi.org/10.1016/j.jmps.2019.03.013.

[37] C. Eberl, R. Thompson, D. Gianola, Digital image correlation and tracking, MATLAB

Cent. File Exch. (2006).

[38] J. Lohner, J.F. Rupprecht, J. Hu, N. Mandriota, M. Saxena, D.P. de Araujo, J. Hone, O. Sahin, J. Prost, M.P. Sheetz, Large and reversible myosin-dependent forces in rigidity sensing, Nat. Phys. 15 (2019) 689–695. https://doi.org/10.1038/s41567-019-0477-9.

[39] Z. Luo, X.A. Zhang, B.A. Evans, C.H. Chang, Active Periodic Magnetic Nanostructures with High Aspect Ratio and Ultrahigh Pillar Density, ACS Appl. Mater. Interfaces. 12 (2020) 11135–11143. https://doi.org/10.1021/acsami.9b18423.

[40] L.Y. Jiang, Y. Huang, H. Jiang, G. Ravichandran, H. Gao, K.C. Hwang, B. Liu, A cohesive law for carbon nanotube/polymer interfaces based on the van der Waals force, J. Mech. Phys. Solids. 54 (2006) 2436–2452. https://doi.org/10.1016/j.jmps.2006.04.009.

[41] A. Needleman, An analysis of tensile decohesion along an interface, J. Mech. Phys. Solids. 38 (1990) 289–324. https://doi.org/10.1016/0022-5096(90)90001-K.

[42] K. Park, G.H. Paulino, Cohesive zone models: A critical review of traction-separation relationships across fracture surfaces, Appl. Mech. Rev. 64 (2011). https://doi.org/10.1115/1.4023110.

[43] B. Chen, P.D. Wu, H. Gao, A characteristic length for stress transfer in the nanostructure of biological composites, Compos. Sci. Technol. 69 (2009) 1160–1164. https://doi.org/10.1016/j.compscitech.2009.02.012.

[44] X. Wei, T. Filleter, H.D. Espinosa, Statistical shear lag model-Unraveling the size effect in hierarchical composites, Acta Biomater. 18 (2015) 206–212. https://doi.org/10.1016/j.actbio.2015.01.040.

[45] T.H. Chang, G. Cheng, C. Li, Y. Zhu, On the size-dependent elasticity of penta-twinned silver nanowires, Extrem. Mech. Lett. 8 (2016) 177–183.

https://doi.org/10.1016/j.eml.2016.03.007.

[46] J. Israelichvili, Intermolecular and surface forces: revised third edition, 2011.

[47] S. Narayanan, G. Cheng, Z. Zeng, Y. Zhu, T. Zhu, Strain Hardening and Size Effect in Five-fold Twinned Ag Nanowires, Nano Lett. 15 (2015) 4037–4044. https://doi.org/10.1021/acs.nanolett.5b01015.

[48] T. Filleter, S. Ryu, K. Kang, J. Yin, R.A. Bernal, K. Sohn, S. Li, J. Huang, W. Cai, H.D. Espinosa, Nucleation-controlled distributed plasticity in penta-twinned silver nanowires, Small. 8 (2012) 2986–2993. https://doi.org/10.1002/smll.201200522.

[49] X.L. Gao, K. Li, A shear-lag model for carbon nanotube-reinforced polymer composites, Int. J. Solids Struct. 42 (2005) 1649–1667. https://doi.org/10.1016/j.ijsolstr.2004.08.020.

[50] D. Kim, S.H. Kim, J.H. Kim, J.C. Lee, J.P. Ahn, S.W. Kim, Failure criterion of silver nanowire electrodes on a polymer substrate for highly flexible devices, Sci. Rep. 7 (2017). https://doi.org/10.1038/srep45903.

[51] H.S. Park, K. Gall, J.A. Zimmerman, Deformation of FCC nanowires by twinning and slip, J. Mech. Phys. Solids. 54 (2006) 1862–1881. https://doi.org/10.1016/j.jmps.2006.03.006.

[52] T. Zhu, J. Li, A. Samanta, A. Leach, K. Gall, Temperature and strain-rate dependence of surface dislocation nucleation, Phys. Rev. Lett. 100 (2008). https://doi.org/10.1103/PhysRevLett.100.025502.

[53] Q. Qin, S. Yin, G. Cheng, X. Li, T.H. Chang, G. Richter, Y. Zhu, H. Gao, Recoverable plasticity in penta-twinned metallic nanowires governed by dislocation nucleation and retraction, Nat. Commun. 6 (2015) 1–8. https://doi.org/10.1038/ncomms6983.

[54] Q. Qin, Y. Zhu, Static friction between silicon nanowires and elastomeric substrates, ACS

Nano. 5 (2011) 7404–7410. https://doi.org/10.1021/nn202343w.

[55] Y. Sun, J.A. Rogers, Structural forms of single crystal semiconductor nanoribbons for high-performance stretchable electronics, J. Mater. Chem. 17 (2007) 832–840. https://doi.org/10.1039/b614793c.

[56] F. Xu, J.W. Durham, B.J. Wiley, Y. Zhu, Strain-release assembly of nanowires on stretchable substrates, ACS Nano. 5 (2011) 1556–1563. https://doi.org/10.1021/nn103183d.

TABLE 1. The identified interfacial parameters for the Ag nanowire/PDMS interfaces in the as-prepared (vdW interactions) and UVO-treated (chemical bonding) cases.

	vdW interactions	**Chemical bonding**
K_0 (TPa/m)	6.0±0.4	135.3±3.2
τ_c (MPa)	2.4±0.1	22.5±1.2
G (J/m^2)	NA	9.5±0.5

TABLE 2. Fracture strains of Ag nanowires calculated from the shear-lag analysis.

		NW Length (μm)	**Fracture strain (%)**
Embedded in as-prepared PDMS	**NW #1**	17.6	1.72
	NW #2	20.3	1.97
	NW #3	9.7	1.84
	NW #4	13.3	1.82
	NW #5	16.5	1.82
On top of UVO-treated PDMS	**NW #1**	11.6	1.62
	NW #2	14.4	2.07 (1st)
		7.3	1.18 (2nd)
	NW #3	15.1	2.13

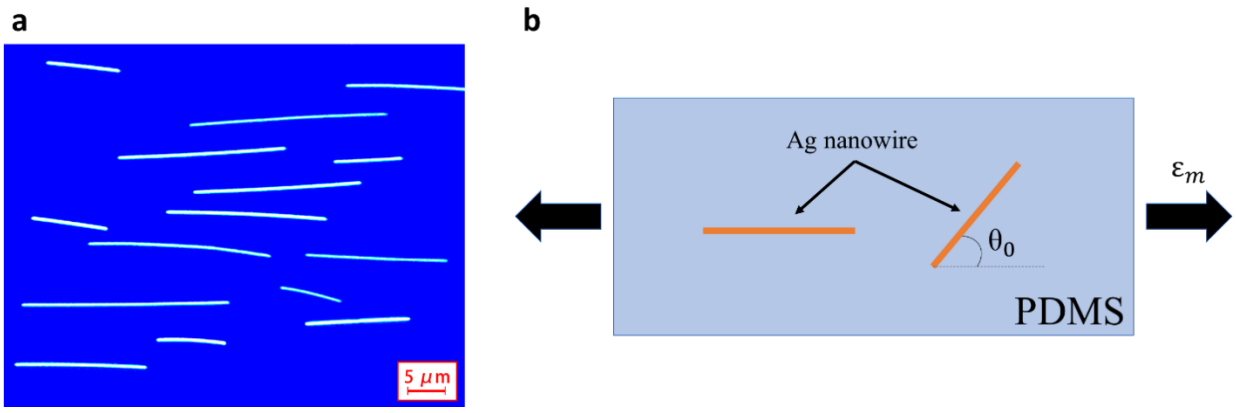

FIG. 1. (a) Optical microscope image showing multiple Ag nanowires on the PDMS substrate with most of them aligned to the loading direction. (b) Schematic of the problem with two representative nanowires: one aligned with the loading direction and the other inclined (initial angle θ_0).

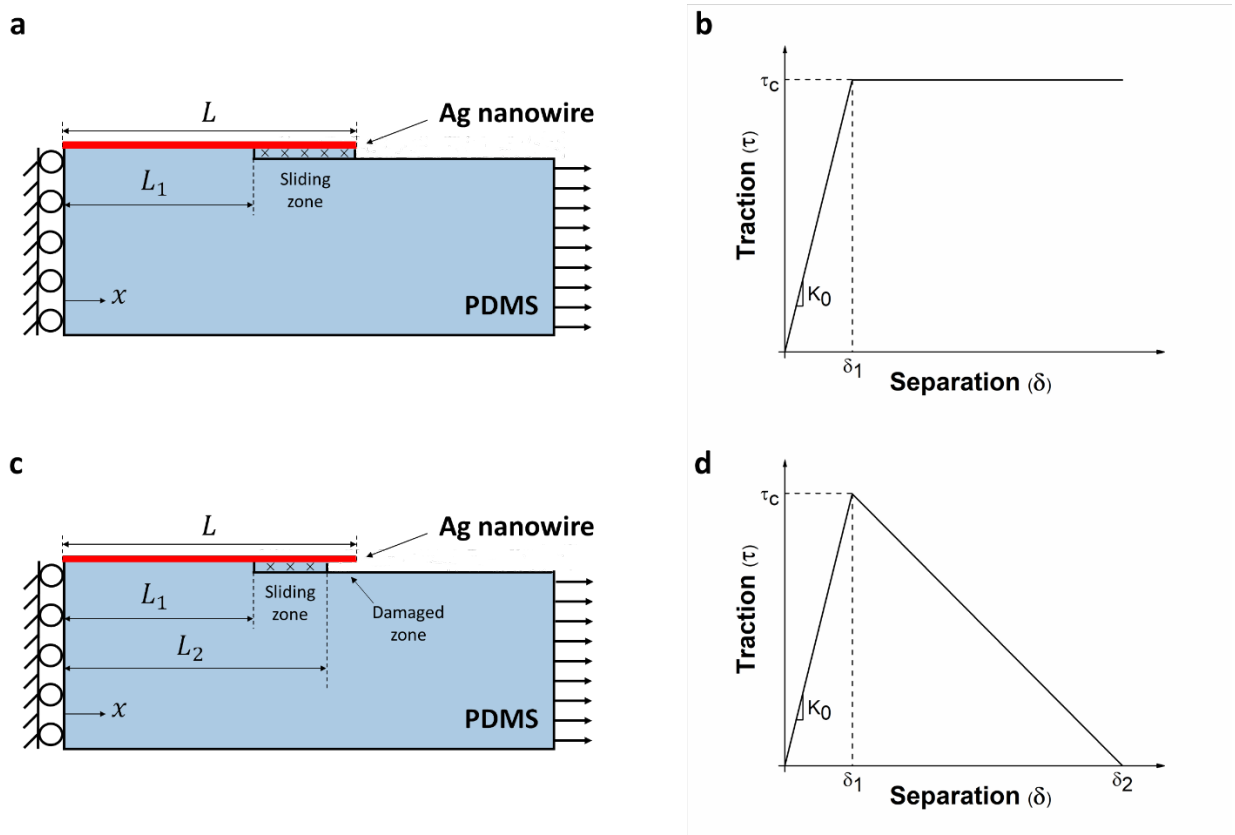

FIG. 2. (a) Schematic of the nonlinear shear-lag model and (b) the corresponding traction-separation law; (c) schematic of the cohesive shear-lag model and (d) the corresponding traction-separation law.

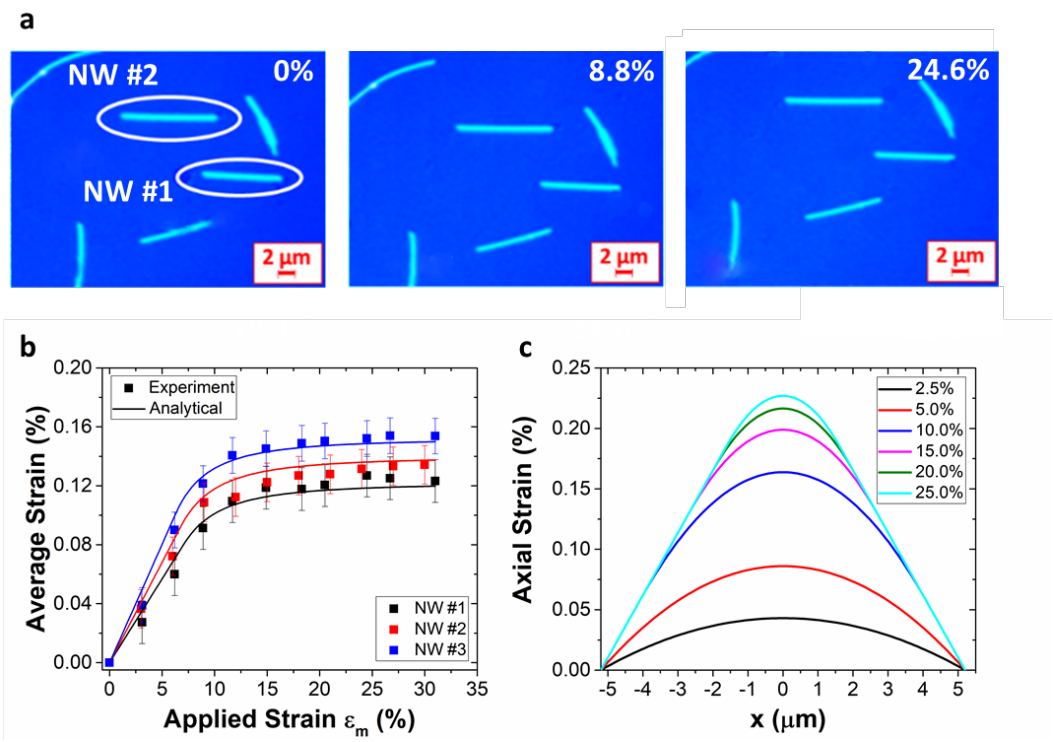

FIG. 3. Results of Ag nanowires on top of as-prepared PDMS. (a) Optical images of NW #1 (10.4 μm long) and NW #2 (12.4 μm long) during the stretching experiment. (b) Fitting experimental data of average nanowire strain for the three Ag nanowires using the nonlinear shear-lag model. (c) Predicted normal strain along the Ag nanowire length for NW #1 for the applied PDMS strain ranging from 2.5 to 25.0%.

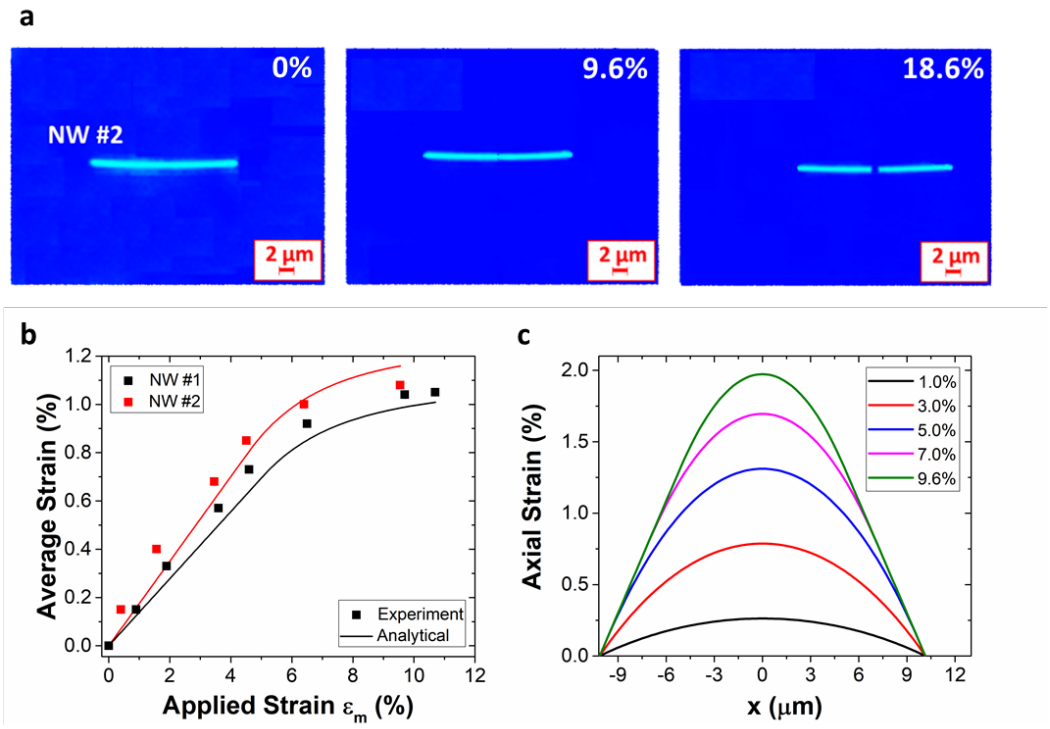

FIG. 4. Results of Ag nanowires embedded in as-prepared PDMS. (a) Optical images of NW #2 (20.3 μm long) during the experiment. (b) Fitting experimental data of average nanowire strain for the two Ag nanowires using the nonlinear shear-lag model. (c) Predicted normal strain along the Ag nanowire length for NW #2 for the applied PDMS strain ranging from 1.0 to 9.6%.

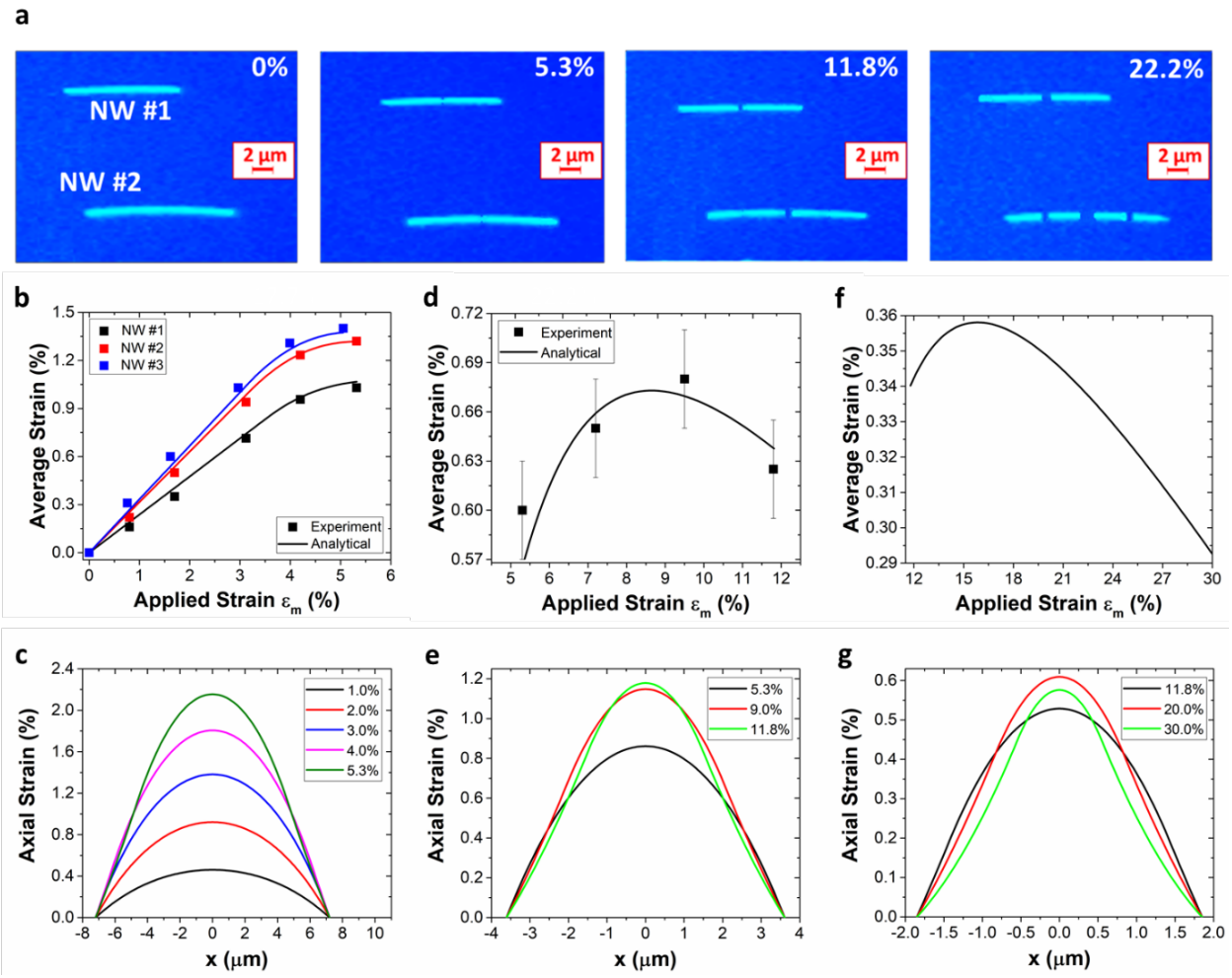

FIG. 5. Results of Ag nanowires on top of UVO-treated PDMS. (a) Optical images of NW #1 (11.6 μm long) and NW #2 (14.4 μm long) during the experiment. (b) Fitting experimental data of average nanowire strain for the three Ag nanowires using the bilinear cohesive shear-lag model. (c) Predicted axial strain along the Ag nanowire length for NW #2. (d) Average nanowire strain of the right segment (7.3 μm long) of NW #2 after the first fracture (experimental data and prediction). (e) Predicted axial strain along the fractured right segment of NW #2 after the first fracture. (f) Predicted average nanowire strain of the right segment (3.6 μm long) of NW #2 after the second fracture. (g) Predicted axial strain along the fractured third segment (from left to right) of NW #2 after the second fracture.

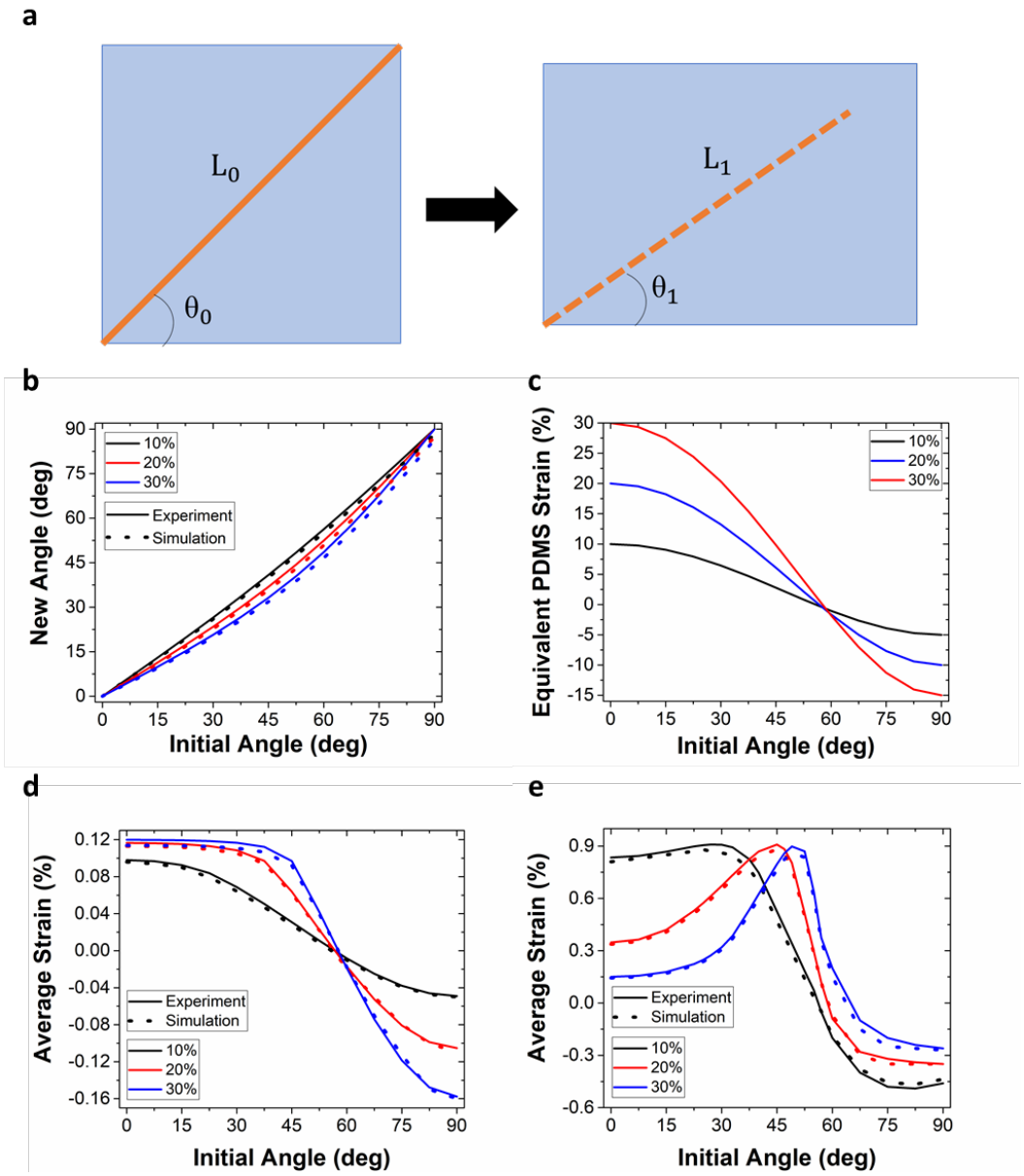

FIG. 6. Results of inclined Ag nanowire on top of PDMS. (a) Schematic of an inclined Ag nanowire on top of PDMS, before and after PDMS stretching. (b) Relationship between initial and new angle for 10, 20, and 30% strain applied to PDMS. (c) Equivalent strain applied to PDMS as a function of initial nanowire angle for 10, 20, and 30% strain applied to PDMS. Average strain of a 10 μm long nanowire as a function of the initial angle in (d) as-prepared and (e) InUVO-treated PDMS. In (d) and (e), the applied axial strain to PDMS is 10%.